NJC

PAPER

View Article Online
View Journal | View Issue

Open Access Article. Published on 06 February 2025. Downloaded on 4/1/2026 5:58:52 PM.
This article is licensed under a Creative Commons Attribution 3.0 Unported Licence.

Check for updates

Cite this: *New J. Chem.*, 2025, **49**, 4178

Probing a conducting polymer by proton-coupled electron transfer of biosimilar redox molecules†

Canyan Che,[ab] Viktor Gueskine,[ac] Martin Sjödin,[d] Alexander Pozhitkov,[e] Liang Yao,[b] Magnus Berggren,[acf] Yuguang Ma,[b] Reverant Crispin[acf] and Mikhail Vagin *[af]

Received 16th December 2024,
Accepted 3rd February 2025

DOI: 10.1039/d4nj04718d

rsc.li/njc

In bioelectronics, the preservation of host homeostasis upon alteration of the electrical charge caused by an implantable electrode has not yet been addressed properly. Here, we propose an *in vitro* strategy to evaluate the appearance of acidic regions in conducting polymer film electrodes due to the hosting of proton-coupled electron transfer (PCET) of bioinspired redox quinone molecules. The effects of electrode-inherent ion transport selectivity as well as the media-inherent buffer capacity on the response of a molecular pH probe, being the quinone redox process, were evaluated using the conducting polymer poly(3,4-ethylenedioxythiophene) (PEDOT). The hosting of the PCET, within the phase of the mixed ion–electron conductor, affects both the surrounding characteristics and the diffusion of the redox molecules. The involvement of di-anion quinone in the primary doping of the conducting polymer results in slowing down its diffusion within the bulk of the porous electrode. The redox process, imposed on the porous electrode in the weakly buffered media, controls the electrode operation *in vivo*. This leads to the appearance of two acidic regions located at the electrode bulk and at the interface between the electrode and the hosting electrolyte, respectively. The proposed methodology is highly relevant for the pre-evaluation of porous electrodes for various (bio-)technological applications.

1 Introduction

The progress in implantable bioelectronics for monitoring, measuring, and transforming electrophysiological and biochemical responses *in vivo* requires the development of soft electrodes in contact with living matter,[1] where the match between the mechanical properties with host tissues is related to the biocompatibility of the electrical implant. In addition, the maintenance of acid–base homeostasis, or a constant concentration of protons is essential for living systems, as an acid–base disorder typically results in pathologic changes and diseases. The *in vivo* proton concentrations are tightly regulated in both extracellular fluids (ECFs) and intracellular fluids (ICFs).[2–5] In the case of ECFs, albumin plays the role of a weak nonvolatile acid, which together with phosphate acts as a buffer. The deviation of ECF's pH from the normal range (7.35 to 7.45) is caused by various disorders.[6,7] Strong electrolyte ions (*e.g.* alkali metal cations and chloride) being present in millimolar concentrations in the ICF appear to be the major determinants of its pH due to the activity of membrane transport proteins, *e.g.* the Na^+/H^+ exchanger, which plays a pivotal role in enzymatic transport of strong electrolyte ions across the cellular membrane, thereby regulating the pH of ICFs.[8] The increased pH of ICFs promotes many cancer-specific activities.[9] From this perspective, we understand that the change of electronic charge of the implanted porous electrode[10] in bioelectronics is compensated by ion transport, which can strongly affect the localized acidity of the host media such as the ECF. Although living organisms have a self-regulation of pH by acid–base homeostasis, these mechanisms are likely limited to maintaining the pH changes upon implantable electrode operation. We believe that such processes imposed on living tissue by *in vivo* bioelectronics should be

[a] *Laboratory of Organic Electronics, Department of Science and Technology, Linköping University, Norrköping 60174, Sweden. E-mail: mikhail.vagin@liu.se; Tel: +46702753087*
[b] *State Key Laboratory of Luminescent Materials and Devices, Institute of Polymer Optoelectronic Materials and Devices, South China University of Technology, Guangzhou 510640, China*
[c] *Wallenberg Wood Science Center, ITN, Linköping University, Norrköping, Sweden*
[d] *Nanotechnology and Functional Materials, Department of Engineering Sciences, The Ångström Laboratory, Uppsala University, Box 534, SE-751 21 Uppsala, Sweden*
[e] *City of Hope National Medical Center, 1500 East Duarte Road, Duarte, CA 91010, USA*
[f] *Wallenberg Initiative Materials Science for Sustainability, Department of Science and Technology, Linköping University, Norrköping 60174, Sweden*

† Electronic supplementary information (ESI) available. See DOI: https://doi.org/10.1039/d4nj04718d

 This journal is © The Royal Society of Chemistry and the Centre National de la Recherche Scientifique 2025

Open Access Article. Published on 06 February 2025. Downloaded on 4/1/2026 5:58:52 PM.
This article is licensed under a Creative Commons Attribution 3.0 Unported Licence.

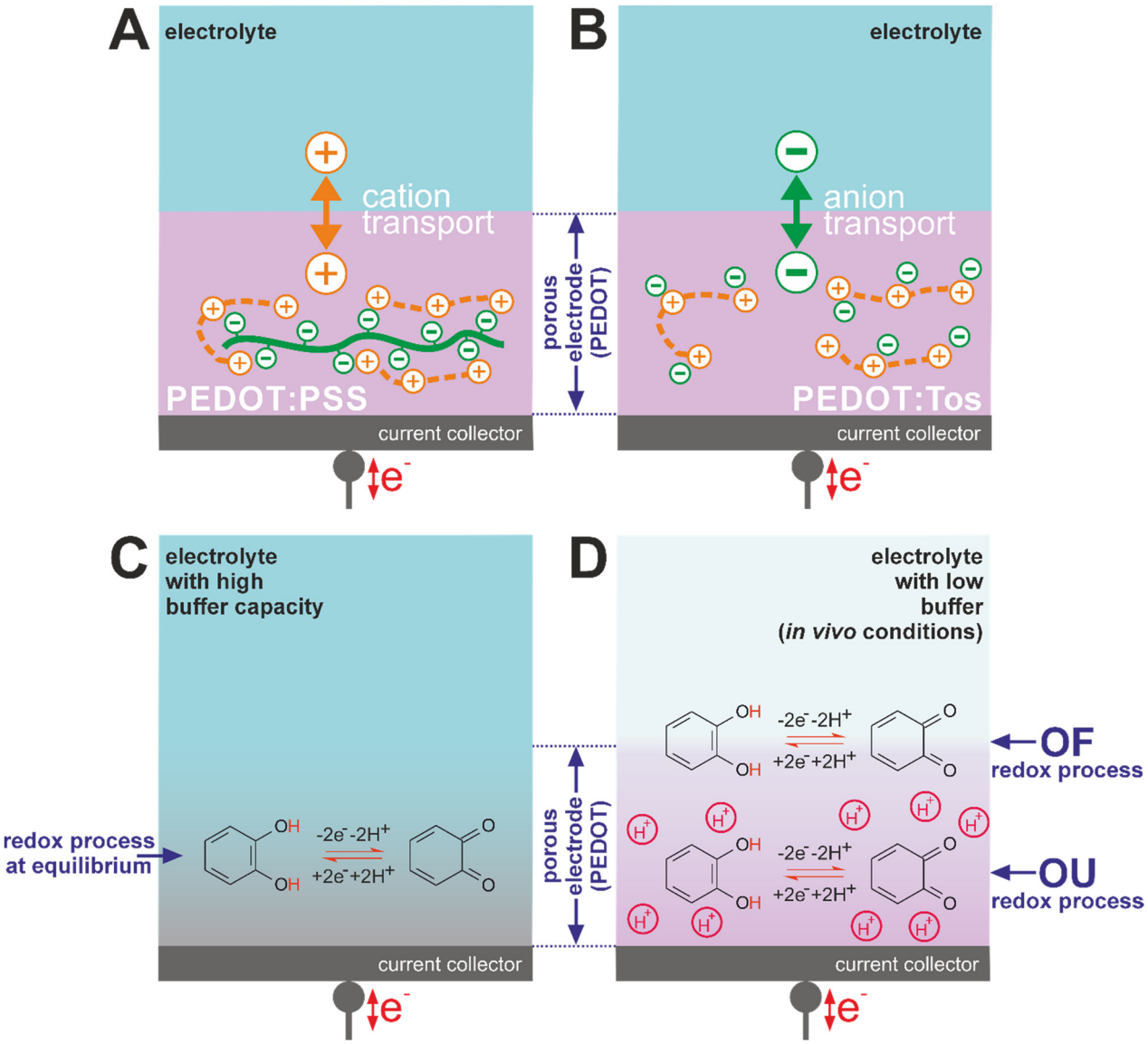

Scheme 1 The cation (A) and anion (B) transport selectivity on the CP; (C) and (D): the effect of buffer capacity on PCET hosted on the CP-based porous electrode.

evaluated by studying the compatibility with the acid–base homeostasis of the host.[11–13]

The molecular porosity of conducting polymers (CPs), enabling the access of ions and reagents to individual backbones,[14–16] enables these organic materials to act as mixed ion–electron conductors (MIECs),[17,18] which are utilized in solid-state ion-selective electrodes.[19] The interface of the porous electrode is a three-dimensional region defined by its boundaries with the electrolyte solution and the current collector. This region, accessible to both ions and electrons, acts as a distinct phase and inherently strives to preserve its electroneutrality. The alteration of either the electrical charge by the external electronic circuit or the ionic charge by the gradient of ion concentration results in the appearance of compensational ionic or electronic transport, respectively.

Specifically, the free positive charge carriers defining the electronic conductivity of the p-type CP phase are compensated by anions, such as the mostly investigated polyethylenedioxythiophene (PEDOT) electrodes. Moreover, the ionic transport species and kinetics differ dramatically due to the counter ion mobility. Compensated by mobile tosylate (Tos), PEDOT:Tos undergoes anion transport upon the modulation of the electronic charge (Scheme 1B), while the one compensated by immobile polystyrene sulfonate (PSS), PEDOT:PSS, presents cation transport behavior (Scheme 1A).[20] Considering that soft biosimilar electrodes help narrow down the mismatch in the mechanical properties between the host tissues and implantable bioelectronics aiming to diminish the immune reaction,[21–29] and that CPs facilitate heterogeneous electron transfer,[30–32] an experimental strategy to evaluate these two

Open Access Article. Published on 06 February 2025. Downloaded on 4/1/2026 5:58:52 PM.
This article is licensed under a Creative Commons Attribution 3.0 Unported Licence.

model porous electrodes with various ionic transport under the conditions modeling *in vivo* is proposed here.

Quinones are redox-active molecules involving proton transport and are the key organic molecules in *in vivo* electron transport chains. This explains the abundance of such molecular electron shuttle systems: the photosystem II,[33,34] ADP-to-ATP oxidative phosphorylation in mitochondria[35] and neurochemistry.[36] Quinones are also popular, low cost, sustainable redox-active additives used extensively in energy devices to enhance the energy density,[37–39] coupled with the conducting polymer matrix due to intrinsic insulating properties.[20,40–42]

Therefore, in this report, the acidity of CP-based porous electrodes was probed under the conditions of controlled ionic transport with redox reactions of two quinone molecules, *i.e.*, catechol and tiron.[43–47] In contrast to hosting media of high buffer capacity, weakly buffered media mimicking the *in vivo* conditions showed the decoupling of the acidity within the interior of the porous electrode from the hosting media. The selectivity of ion transport on porous electrodes defined by the mobility of the primary dopant affects the kinetics of the redox process. The proposed experimental approach can be utilized in pre-tests of electrodes implanted in living organisms.

2 Results and discussion

Films of PEDOT:Tos and PEDOT:PSS deposited onto a current collector (glassy carbon (GC)) were used as a general model of porous electrodes. PEDOT is archetypical among CPs due to its high electronic conductivity (up to 1000 S cm^{-1})[48] and processability. The high conductivity of PEDOT at the potential region of the quinone redox process is independent of the pH. The sluggish kinetics of catechol redox conversion on blank glassy carbon (Fig. S1, ESI†)[46] illustrate the inertness of the current collector. The transport of chemical species within the porous electrode is assured by both diffusion into the pores and coulombic forces induced on ions to compensate for the electrical charge inside the MIEC. The selectivity of transport towards the anions or the cations is defined by the mobility of ionic species virginally present in the MIEC phase for the compensation of free carriers of electronic charge, the so-called primary dopants.

3 Thermodynamics

3.1 Standard conditions: proton transfers at the inherent acid–base equilibria

The redox reaction of quinones in protic solvents including water involves transfers of both electrons and protons and can be represented as:

$$Q + nH^+ + 2e^- \leftrightarrow C(H^+)_n \quad (1)$$

where n, the number of protons involved, can be 0, 1, or 2 depending on the pH. If n is equal to 1 or 2, then reaction (1) proceeds *via* PCET. Considering only mono- or bi-molecular reactions as elementary steps, the enumeration of any possible

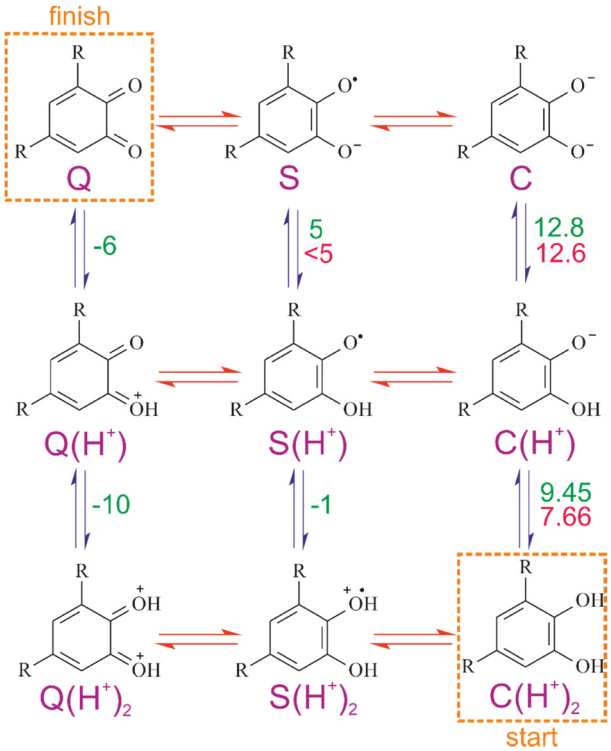

Scheme 2 Scheme of squares of oxidation for catechol (R = −H) and tiron (R = $-SO_3^-$); pK_a values for catechol[51–56] and tiron[57] are green and red, respectively; red (horizontal) and blue (vertical) routes represent the elementary electron and proton transfers, respectively.

intermediates gives a nine-membered scheme of squares (Scheme 2) as a mechanism of reaction (1).[43,49,50] Deprotonation of $C(H^+)_n$ facilitates its oxidation thermodynamics as soon as the proceeding of reaction (1) from right to left becomes easier.

The achievement of inherent acid–base equilibria upon the coupled proton transfers (vertical routes at Scheme 2) during reaction (1) is assured in voltammetry experiments using an aqueous electrolyte of high buffer capacity. The outcome of such conditions is the so-called Nernstian behavior of equilibrium potential: the dependence of the equilibrium potential of (1) on the pH, the so-called Pourbaix diagram, is linear with a slope of $-\left(\frac{n}{2}\right) \times 0.059$ V per pH unit. Indeed, in the media of high buffer capacity, we observed, by voltammetry experiments, that the increase of pH led to a shift of the peak current potentials as well as the equilibrium potential of the redox process in the negative (cathodic) direction for all the systems utilized in this study (*e.g.* for the catechol redox process on a PEDOT-based blend with polystyrene sulfonate (PEDOT:PSS), Fig. 1).

The Pourbaix diagram for a certain redox process allows (i) the Nernstian diagnostics of the number of protons involved and (ii) the evaluation of the solvation properties of the solvent. Specifically, (i) the slopes of pH dependence of the equilibrium potential are 0.059 V (pH unit)$^{-1}$, 0.030 V (pH unit)$^{-1}$ and 0 V (pH unit)$^{-1}$ for n of 2, 1 and 0, respectively, while (ii) the pH

 This journal is © The Royal Society of Chemistry and the Centre National de la Recherche Scientifique 2025

Open Access Article. Published on 06 February 2025. Downloaded on 4/1/2026 5:58:52 PM.
This article is licensed under a Creative Commons Attribution 3.0 Unported Licence.

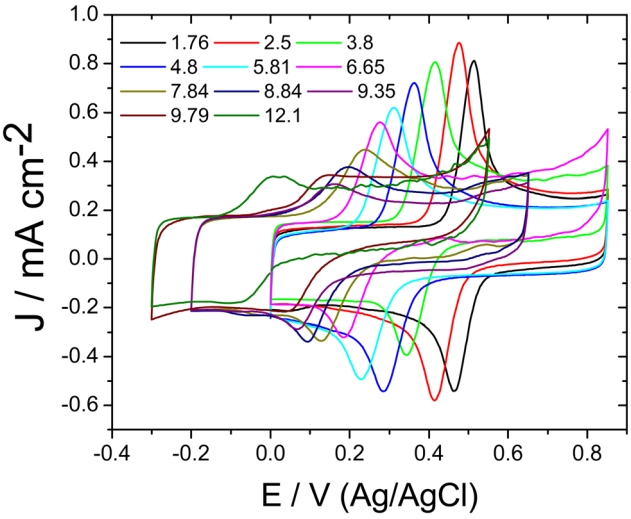

Fig. 1 The maintenance of reversibility for the catechol redox process on the PEDOT:PSS-modified GCE. The voltammograms were recorded in 1 mM catechol solution in buffered background electrolytes (pH 1.7–12.1; 20 mV s^{-1}).

values where the switching between the slopes takes place identifies the acid dissociation constants.

3.1.1 Catechol. The inherent acid–base equilibria of quinones, namely, their first and the second acid dissociation constants in water, are:

$$K_1 = \frac{[C(H^+)][H^+]}{[C(H^+)_2]} \quad (2)$$

and

$$K_2 = \frac{[C][H^+]}{[C(H^+)]} \quad (3)$$

where [C], [C(H$^+$)], [C(H$^+$)$_2$] and [H$^+$] are the concentrations at the equilibrium. For catechol, $-\log(K_1)$ = pK_1 9.45 and pK_1 12.8,[51] define the pH points where the switching of n of 2-to-1 and 1-to-0, respectively, takes place in solution. Essentially, at low pH values the catechol redox process on PEDOT films of different compositions (Fig. 2A and B) showed full coincidence of equilibrium potentials with a Nernstian slope for n = 2 (namely, 0.059 V (pH unit)$^{-1}$) illustrating the identity of the acid–base equilibria established outside and inside the porous electrode phase (Scheme 1C). On the other hand, the pH values of the switching points are significantly affected by the porous electrode materials. With PEDOT:PSS, reaction (1) with n = 2 spans almost the entire studied pH range (Fig. 2A). This implies that the switching pH points with this porous film are significantly shifted to deeply alkaline external media in comparison with the same reaction driven on the smooth electrode surface in water. In contrast, the catechol redox process on PEDOT:Tos (Fig. 2B) showed that the switching pH points shifted to acidic media (2-to-1: at pH 6.7, 1-to-0: at pH 9.6) in comparison with the surface reaction in bulk water (2-to-1: at pH = pK_1; 1-to-0: at pH = pK_2). The influence of the electrode composition on the switching pH points witnesses two aspects of the redox process

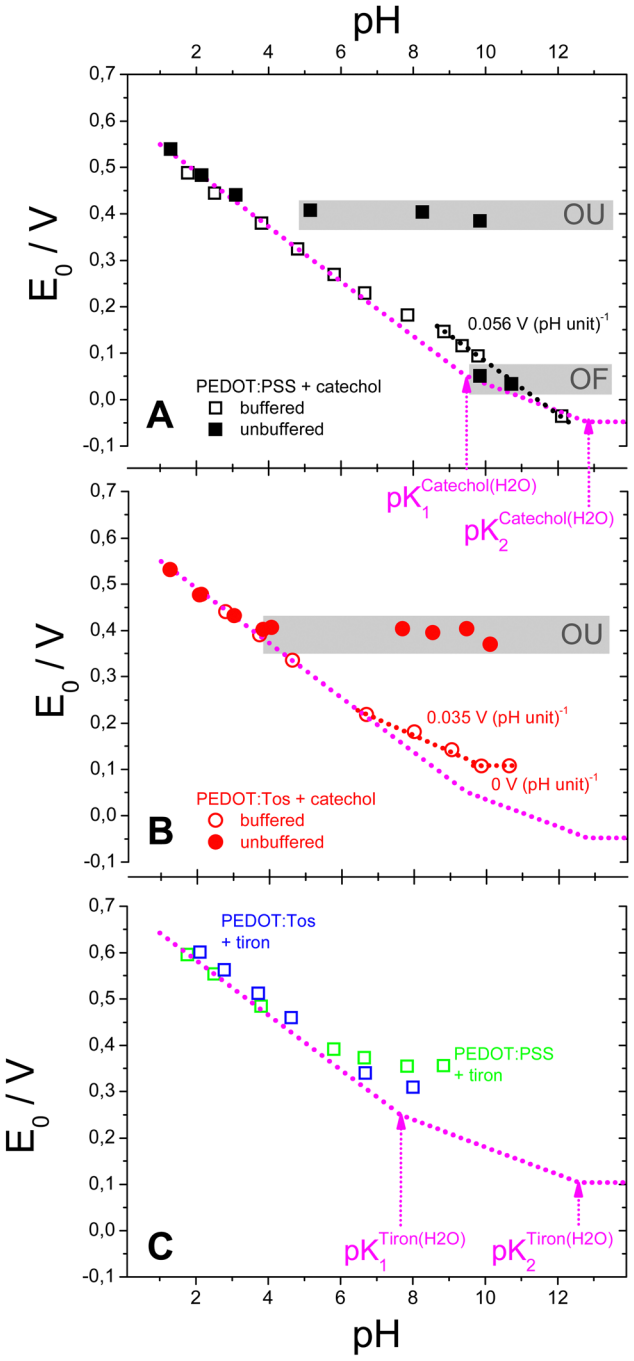

Fig. 2 Pourbaix diagrams of proton-coupled electron transfer reactions on conducting polymers. The pH dependencies of midpoint potentials of redox processes of catechol on PEDOT:PSS and PEDOT:Tos ((A) and (B), respectively) and tiron (C) on both PEDOT:PSS- and PEDOT:Tos-films in buffered and unbuffered electrolyte solutions (open and filled symbols, respectively); OU and OF are midpoint potentials of oxidation-unfavorable and oxidation-favorable processes.

on the porous electrode. (A) The catechol redox process takes place in the porous electrode interior, which is illustrated by the dependence on the catechol redox currents on the thickness of PEDOT films (Fig. S2, ESI†). (B) The inherent acid–base equilibria of catechol (vertical routes of Scheme 2) are affected.

Open Access Article. Published on 06 February 2025. Downloaded on 4/1/2026 5:58:52 PM.
This article is licensed under a Creative Commons Attribution 3.0 Unported Licence.

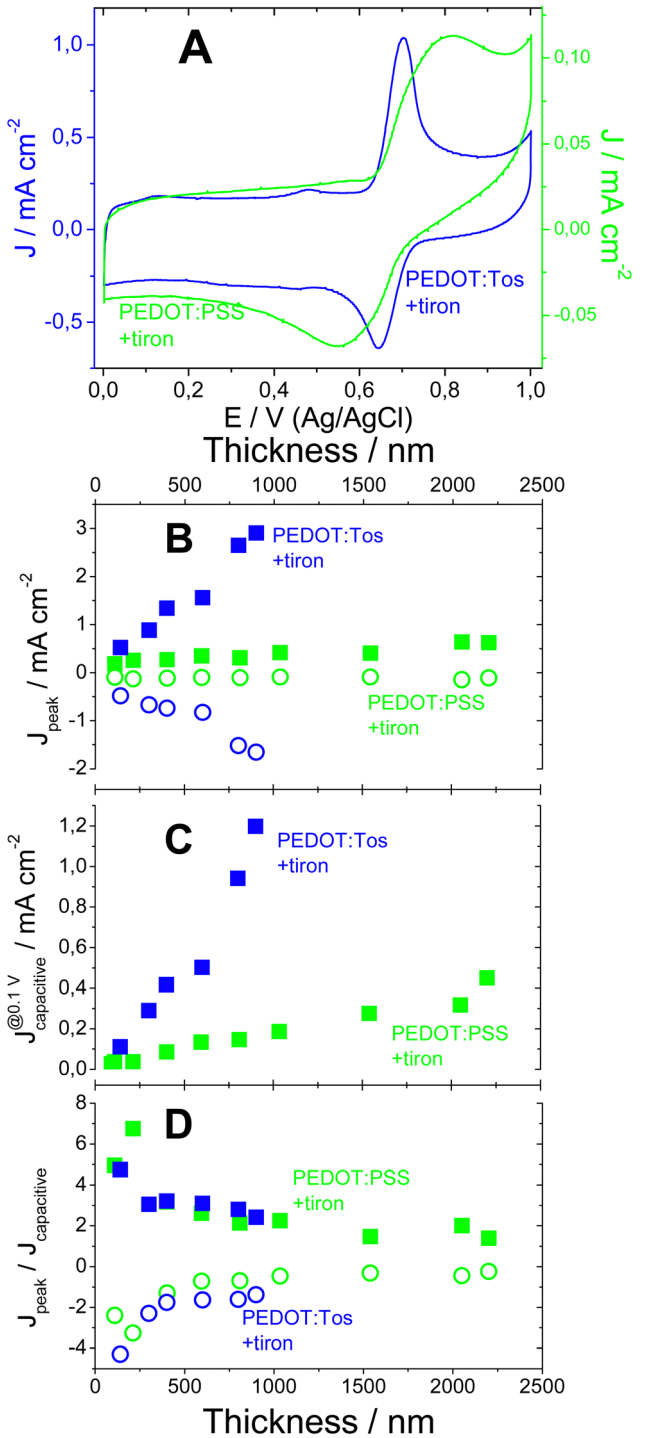

Fig. 3 The dopant-dependent selectivity of the MIEC to the redox process of quinone di-anion. (A): cyclic voltammograms acquired on PEDOT:PSS and PEDOT:Tos-modified electrodes in the presence of tiron (1 mM, pH 2, high buffer capacity); thickness dependencies of the redox peak currents of tiron, the capacitive currents on PEDOT films and redox peak currents of tiron normalized on the capacitive currents (B), (C) and (D), respectively).

This could be due to three reasons. (i) Polarity of the polymer interior is different from the water in the bulk. Both protons and pristine catechol can be excluded from the species affected by the solvation due to the intactness of the proton energetics illustrated by the coincidence of equilibrium potentials with Nernstian slopes and the neutrality of non-dissociated catechol, respectively. Therefore, the acidic or alkaline shifts of switching pH points observed on PEDOT:Tos or PEDOT:PSS films, respectively (Fig. 2A and B), could witness that the environment inside these porous electrodes is more polar or less polar than the bulk water, respectively. (ii) The pH inside the porous electrode could be affected by the ion selectivity of the porous film towards the acidic or basic components of the buffer. (iii) The involvement of de-protonated forms of catechol in the primary doping of PEDOT:Tos, namely, in the stabilization of positive charge carriers of PEDOT:Tos.

Coherently, the ionic selectivity of the CP affects the stability of the redox probe. The catechol redox process in aqueous media at the smooth (inert) interface, such as blank GC, leads to the irreversible redox behavior of catechol already at a pH above 9 due to the nucleophilic attack on the catechol oxidation product, namely, *o*-benzoquinones by hydroxyl anions *via* the Michael addition reaction.[58–60] The porous interior of cation-transporting PEDOT:PSS leads to protection of the catechol probe and stabilization of the *ortho*-benzoquinone against nucleophilic attack, represented by the extension of the catechol redox reversibility in the voltammogram up to pH 12 (Fig. S3A, ESI†). In contrast, the interior of the anion-transporting PEDOT:Tos interface leads to deprotonation of catechol, and destabilization of the *ortho*-benzoquinone against nucleophilic attack, which is illustrated by interruption of the reversibility in the voltammogram at pH 12 (Fig. S3B, ESI†), correspondingly.

The reversibility of the catechol redox process on PEDOT:PSS can be attributed to the selective transport of cations into the bulk of the conducting polymer (CP), while access for nucleophiles, such as anions that could attack quinones, is effectively restricted. Unlike aliphatic sulfonates, such as those in Nafion,[61] the nucleophilic reactivity of aromatic sulfonates, such as those in PSS, is significantly suppressed. This demonstrates how controlling the ionic transport can influence the chemical reactivity within the bulk of a porous electrode.

3.1.2 Tiron. The redox process of the di-anion tiron shows higher selectivity towards the PEDOT electrode composition in comparison with the redox behavior of neutral catechol. The tiron redox process on anion-transporting PEDOT:Tos achieves a high degree of reversibility and yields one order of magnitude higher peak currents in comparison with a similar process on cation-transporting PEDOT:PSS. This could be explained by the coulombic interactions between the redox probe and primary dopant of PEDOT (Fig. 3A). A significant effect of the PEDOT film composition on the thickness dependences of redox peak currents is also visible (Fig. 3B). Redox peak currents of tiron scale up linearly with the PEDOT:Tos thickness, while a similar process is almost independent of the thickness of PEDOT:PSS. This implies that the access to the film interior of the redox process of di-anion tiron is significantly affected by the initial primary dopant, PSS or Tos.

The slower diffusion of tiron was observed on anion-transporting PEDOT:Tos in comparison with cation-

 This journal is © The Royal Society of Chemistry and the Centre National de la Recherche Scientifique 2025

Open Access Article. Published on 06 February 2025. Downloaded on 4/1/2026 5:58:52 PM.
This article is licensed under a Creative Commons Attribution 3.0 Unported Licence.

transporting PEDOT:PSS, which is an origin of observed selectivity. This is illustrated by lower diffusional currents of the tiron redox process on PEDOT:Tos in comparison with PEDOT:PSS (Fig. 3A, oxidation currents at diffusion control: *ca.* 0.9 V; reduction currents at diffusion control: *ca.* 0.4 V). Coherently, the slow diffusion of tiron on PEDOT:Tos is visible in voltammetry experiments on a rotating disk electrode (RDE; Fig. S4A, ESI†). The increase of rotation speed resulted in the conservation of the peak current of tiron oxidation on PEDOT:Tos, which disabled the use of Levich analysis in the estimation of the diffusion coefficient (Supporting Note S1, ESI†). The diffusion coefficient estimated for tiron oxidation on PEDOT:PSS was 3.6×10^{-6} cm^2 s^{-1}.

In contrast to di-anion tiron, neutral catechol shows indiscrimination of the redox behaviour towards the PEDOT film composition (*e.g.* similar thickness dependencies on PEDOT:PSS and PEDOT:Tos, Fig. S2, ESI†) and higher diffusion coefficients (8–10 $\times$ 10^{-6} cm^2 s^{-1}) in comparison with tiron. These facts allows us to hypothesize that di-anion tiron is involved in the compensation of positive charge carriers within the phase of PEDOT:Tos, *i.e*, the primary doping of PEDOT by tiron. The alteration of electronic charge within the MIEC phase of dopant-exchangeable PEDOT:Tos is equilibrated by the transport of anions, such as tiron. On the contrary, the doping of PEDOT with an excess of immobile poly-anion PSS results in the change of ion transport selectivity to cations.

Regardless of the composition, the capacitive currents on PEDOT-modified electrodes (*e.g.* at 0.2–0.3 V, Fig. 3A) scale linearly with the film thickness (Fig. 3C). This implies that the capacitive currents can represent the electrochemical active surface area (EASA), namely, the surface area of the CP hosting the electrical double layer formed by the ions of the background electrolyte. The slope of the thickness dependence of PEDOT:Tos is more than 7 times higher than the slope of PEDOT:PSS. The lower volumetric capacitance observed for PEDOT:PSS could be due to the presence of both an excess of the electronic insulator PSS[62] and water inside the CP film. Assuming the intactness of the density of states defining the heterogeneous electron transfer on the electronic conductor, one can conclude that PEDOT:Tos has more than 7 times larger EASA than PEDOT:PSS. The normalization of the peak currents of the tiron redox process recorded on CP films of different thicknesses (Fig. 3B) on the corresponding capacitive currents allows the evaluation of the effect of EASA on the redox process. The close similarity of the thickness dependences of tiron peak currents observed for PEDOT:PSS and PEDOT:Tos (Fig. 3D) implies the identity in the density of states for heterogeneous electron transfer on both CP films and the absence of any catalytic phenomena created upon the change of the primary dopant.

The thermodynamics of the tiron redox process is affected by its involvement in the primary doping of PEDOT. The significant acidic shifts of the switching pH points are visible in the Pourbaix diagram of the tiron redox process on PEDOT:Tos (Fig. 2C) in comparison with inherent acid–base equilibria for tiron in bulk water (pK_1 7.66, pK_2 12.6[57]).

To sum up, the composition of PEDOT films with the mobile or immobile anions, *i.e.* Tos or PSS as primary dopants, respectively, affects the thermodynamics of the proton-coupled electron transfer of quinones (reaction (1)). The quinone redox process on PEDOT films, as a model of the porous electrode, is affected by the ionic transport that appeared upon the alteration of the electronic charge of the film. The solvation properties and the reactivity of water are altered by the porous electrode.

3.2 *In vivo* conditions: low buffer capacity

The high buffer capacity of the quinone solution during the investigation of redox process is essential to observe the effect of the inherent acid–base equilibria on the thermodynamics of reaction (1). In contrast, under the conditions of low buffer capacity of the outer background electrolyte,[63] particularly relevant for the electrodes implanted *in vivo*,[22,24] the decoupling of the porous electrode phase from the outer electrolyte is expected.

3.2.1 Catechol. First, consider 1 mM catechol solution in a weakly acidic electrolyte (pH $>$ 3) of low buffer capacity. The concentration of catechol is higher than the concentration of protons ([H$^+$] $<$ 1 mM). Notably, the observed redox potentials of catechol that do not suggest the establishment of thermodynamic equilibrium, on both PEDOT:PSS and PEDOT:Tos, become almost pH-independent (Fig. 2A and B, respectively, filled symbols). The value of pH, at which the behavior of buffered and unbuffered systems starts to diverge, is 2.7 (Fig. 2A and B). This pH value is recorded by electrochemical methods and is defined by the protons (2 mM) released during catechol oxidation within the phase of the porous electrode. Note that this electrode-localized pH is lower than the pH at the bulk of the electrolyte.

Second, consider the pH dependence of the catechol redox process on both PEDOT:PSS and PEDOT:Tos obtained in the electrolyte of low buffer capacity at a moderate to a high pH (Fig. 2A, B (filled symbols) and Fig. S6A, B, ESI†). The peak currents visible at potentials around 0.4 V (Fig. S6, ESI†) start losing their intensity with an increase in the pH. At *ca.* pH $>$ 9 the change is profound: the redox peak at 0.4 V disappears completely, while a new reversible redox process appears at close to 0 V. We will define redox processes at 0.4 V and 0 V as oxidation-unfavorable (OU) and oxidation-favorable (OF), respectively.

The interim character of the OF process, as an indication of its far-from-equilibria origin, is shown by two aspects: (i) the OF process disappears with the increase of the scan rate of voltammetry (*e.g.* catechol on PEDOT:Tos Fig. 4) and (ii) the redox peak currents of the OF process decrease with the increase of buffer capacity.[64] These facts exclude the assignment of the OF process either to pH-independent redox process of catechol dianion (C, Scheme 2) or to the redox reactions of products of single electron oxidation of catechol, namely, the semi-quinone radical family (S(H$^+$)$_2$, S(H$^+$) and S, Scheme 2).

It is believed that both OF and OU processes involve redox reactions of intact catechol as a starting reagent (Scheme 2)

Open Access Article. Published on 06 February 2025. Downloaded on 4/1/2026 5:58:52 PM.
This article is licensed under a Creative Commons Attribution 3.0 Unported Licence.

located at the film surface, namely, at the PEDOT/aqueous electrolyte interface, and at the bulk of the PEDOT film, respectively (Scheme 1D). The slower diffusion within the pores of the PEDOT film can lead to the slower diffusion observed for the OU process in comparison with OF. This is supported by higher diffusional currents of oxidation for the OF process (*e.g.* at 0.2 V, Fig. S6A, ESI†) than for the OU process (*e.g.* at 0.6 V, Fig. S6A, ESI†). The different diffusional behavior of redox processes located at the surface (OF) and at the bulk of the film (OU) results in square root and linear dependencies on the scan rate, respectively. Indeed, the voltammetry at slow scan rates shows the appearance of the OF process of catechol on PEDOT:Tos (Fig. 4), even in a highly acidic 0.1 M H_2SO_4 solution of low buffer capacity. The increase of the scan rate leads to the disappearance of the OF process (Fig. 4). The long time of the experiment at a slow scan rate allows the protons released within the porous electrode to be neutralized. In such a scenario, the part of the film that is close to the PEDOT/aqueous electrolyte interface is available for slow neutralization, while the bulk of the film remains acidified by released protons (Scheme 1D). This leads to the observation of OF and OU processes illustrating neutralized and acidified parts of the film.

3.2.2 Tiron. Regardless of the PEDOT composition, the pH dependence of the tiron redox process on electrolytes of low buffer capacity showed the co-existence of OF and OU processes (Fig. S6C, D and S7, ESI†). This is in stark contrast to catechol where only one process is observed (Fig. 2A, B and Fig. S6A, B, ESI†). Considering the significantly slower diffusion of tiron dianion on the PEDOT film in comparison with catechol, one can hypothesize that the OF–OU coexistence observed for the tiron redox process in the electrolyte of low buffer capacity has diffusional origin. The fast diffusion of catechol could result in the presence of the OU process even at the surface of the film, which leads to OF process disappearance. On the contrary, the slower diffusion of tiron enables the presence of the OF redox process. Therefore, the zones of the films where the OF and OU redox processes take place are different for catechol and tiron. Coherently, the involvement of tiron in the primary doping of PEDOT:Tos slows down its diffusion, which leads to the appearance of the surface OF redox process at a lower pH value (*ca.* pH 4, Fig. S7B, ESI†) in comparison with the similar process on PEDOT:PSS (*ca.* pH 6.5, Fig. S7A, ESI†).

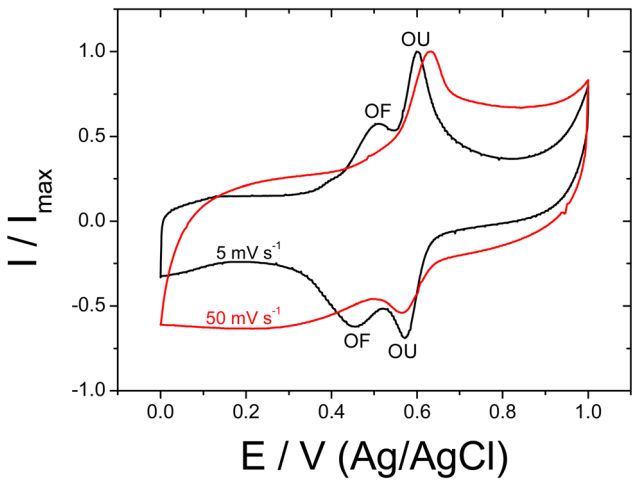

Fig. 4 The kinetic control of released proton neutralization during the catechol redox process in the neutral electrolyte of low buffer capacity. The voltammograms normalized by the oxidation peak currents of catechol (1 mM in 0.1 M H_2SO_4) recorded on PEDOT:Tos film-modified glass slides at scan rates of 5 mV s^{-1} and 50 mV s^{-1} (black and red curves, respectively).

4 Oxidation kinetics

The kinetics of catechol and tiron oxidation was evaluated by voltammetry at the PEDOT-modified RDE. The diffusion limitation observed on RDE measurements for tiron oxidation on PEDOT:Tos (Fig. S4A, ESI†) motivates the assumption that the hydrodynamic voltammetry probes the oxidation reaction at both the surface and the bulk of the PEDOT film. High buffer capacity media served to assure that the acid–base equilibria are effectively established. The analysis of voltammograms obtained on the RDE was based on the Koutecky–Levich equation supposing the kinetic control of the electrode reaction (Supporting Note S1, ESI†).

The standard rate constants of the electron transfer for catechol and tiron oxidation on porous electrodes in well-buffered solutions obtained as described above (Fig. 5A and B, respectively) were found to change non-monotonously with the pH. According to E. Laviron,[50] the slope of dependences of the logarithm of the standard rate constant on the pH is ±0.5 (dashed lines in Fig. 5A and B), provided all the inherent acid–base equilibria (vertical routes of Scheme 2) are established. Our results for the oxidation of neutral catechol on cation-transporting PEDOT:PSS (Fig. 5A) agree with this prediction only in a limited range of pH values (pH 6–10), which suggests the achievement of acid–base equilibria. On the contrary, at the anion-transporting PEDOT:Tos, the Lavironian behavior was not observed in the entire pH range of this study. A possible explanation of this difference could be the effect of selectivity of ion transport, cations (protons) for PEDOT:PSS, and anions for PEDOT:Tos, on the neutralization of released protons. Coherently, the significant effect of ion transport selectivity (PEDOT:PSS *vs.* PEDOT:Tos) on the standard rate constant was observed for dianion tiron (Fig. 5B), while the oxidation of neutral catechol remains almost unaffected (Fig. 5A). These facts support our concept of ion-selective electrocatalysis.[65]

An attempt was made to simulate the archetypical reversible cyclic voltammetry of the quinone redox process observed on stagnant smooth electrodes using well-reputed DigiSim software and the full scheme of squares (Scheme 2) with the thermodynamics, namely, equilibrium potentials and acid dissociation constants, listed by R. Compton *et al.*[52] Strikingly, for any choice of rate constant values for the electron transfer and rates of protonation spanning many orders of magnitude, even a qualitative agreement with the shape of cyclic

 This journal is © The Royal Society of Chemistry and the Centre National de la Recherche Scientifique 2025

Open Access Article. Published on 06 February 2025. Downloaded on 4/1/2026 5:58:52 PM.
This article is licensed under a Creative Commons Attribution 3.0 Unported Licence.

voltammograms observed in an experiment (*e.g.* Fig. 1) could not be obtained at any pH and scan rate (data not shown), leave alone pH dependence. It is noteworthy that R. Compton *et al.*[52] themselves were able to fit the experimental cyclic voltammograms only in a limited range of pre-defined pH values, independent of each other, as two effective inverted single-electron transfers, leaving aside the experimental pH dependence and explicit treatment of proton transfers (then the primary acid–base equilibria are introduced as the ratio between the rates of the forward and backward elementary

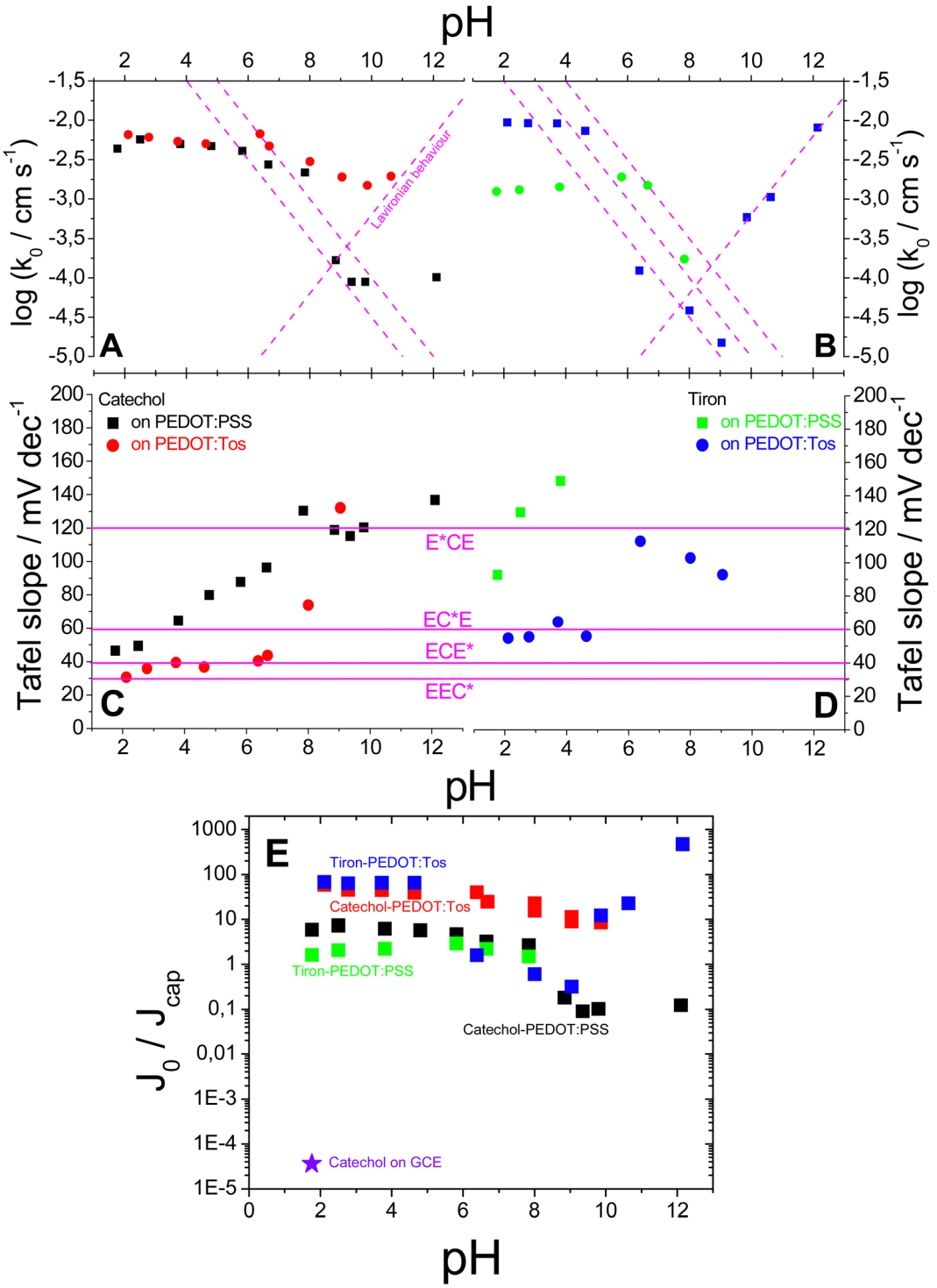

Fig. 5 The pH dependencies of standard rate constants and Tafel slopes of catechol ((A) and (C), respectively) and tiron ((B) and (D), respectively) oxidation on PEDOT:Tos and PEDOT:PSS in Britton–Robinson buffers; (E) the pH dependencies of the exchange current densities of catechol-on-PEDOT:PSS-, catechol-on-PEDOT:Tos-, tiron-on-PEDOT:Tos- and tiron-on-PEDOT:PSS-modified GC normalized by capacitive current densities in buffered electrolytes. ★ - catechol oxidation on the GC.

Open Access Article. Published on 06 February 2025. Downloaded on 4/1/2026 5:58:52 PM.
This article is licensed under a Creative Commons Attribution 3.0 Unported Licence.

proton transfers). It is supposed that such a critical negative result illustrates the proceeding of reaction (1) *via* concerted proton electron transfers corresponding to the diagonal transitions in the scheme of squares, *e.g.* direct $C(H^+)_2$-to-$S(H^+)$ and direct $S(H^+)$-to-Q (Scheme 2). Such a mechanism is explicitly excluded from the scheme of squares as well as from the DigiSim algorithm. Concerted proton electron transfers are not considered in Lavironian kinetics with its explicit assumption of infinitely fast rates of proton transfers, compared to the rates of electron transfer. Moreover, Laviron's assumption of fast proton equilibria is questionable for weak acids like quinones, since their dissociation and association reactions (vertical path in Scheme 2) may not be fast enough to maintain equilibrium.

The Tafel slope, which might be simplified as a voltage loss due to the slow electrode reaction kinetics, increases with growing pH for all electrode reaction systems (Fig. 5C and D). This illustrates the change of the rate-determining step (RDS) of oxidation due to the kinetic effect of proton transfers. The overall oxidation of quinones at pH values allowing $n = 2$ or 1 (reaction (1)) suggests the existence of a chemical step (C), namely, de-protonation between two single electron transfers (E): the ECE mechanism. The increase of the Tafel slope observed upon increasing the pH led to a shift of the RDS from the second electron transfer, namely, the ECE* mechanism (where * denotes the RDS; Tafel slope: $\frac{40}{1-\frac{\Delta}{3}}$ mV dec^{-1}, where Δ is an overpotential-dependent constant)[66] to the early individual reaction steps, such as C (yielding EC*E; Tafel slope: 60 mV dec^{-1}).[66] Among all systems of study, only tiron oxidation on PEDOT:Tos (Fig. 5D) showed the conservation of the EC*E mechanism in a pH range between 2 and 5, which might be a result of the additional equilibria imposed on tiron due to the involvement into the PEDOT doping.

To consider the effect of the porous electrode surface, the exchange current densities were normalized by the capacitive current densities,[67] which represent EASA (Fig. 5E). Assuming the equal specific capacitance of all PEDOT films of study, it is possible to confirm the effect of ion transport selectivity on the rate of the heterogeneous transfer on quinones. The appearance of ion-selective electrocatalysis in the oxidation of di-anionic tiron yields more than 30 times higher surface-normalized exchange current at anion-transporting PEDOT:Tos compared to that at cation-transporting PEDOT:PSS at pH 2. For neutral catechol oxidation at PEDOT:Tos *vs.* PEDOT:PSS, the increase is smaller: 6 times at pH 2.5 in the absence of ion-selective electrocatalysis. Essentially, the catechol oxidation on the smooth GC showed the lowest values of roughness-normalized exchange currents in comparison with the porous electrodes of conducting polymers.

5 Conclusions

Organic redox processes involving PCET were utilized as calibration-free pH probes to examine the interior of a conducting polymer, serving as a model for soft implantable electrodes. The di-anionic quinone participates in the primary doping of the MIEC, influencing its diffusion within the porous electrode phase and defining the redox process selectivity relative to dopant-dependent ionic transport in the conducting polymer. The high buffering capacity ensures pH conservation both inside and outside the porous electrode, while the Nernstian mechanistic transitions of PCET are modulated by the electrode environment.

Selectivity of ionic transport further impacts the chemical reactivity within the interior of the porous film. In weakly buffered host media, designed to mimic *in vivo* microenvironments, two localized acidic regions emerge: one within the bulk of the porous electrode and another at the interface between the electrode and the external electrolyte. It is proposed that this experimental approach holds broad relevance for porous electrodes in various technological applications.

6 Experimental section

6.1 Reagents

All inorganic salts, 3,4-ethylenedioxythiophene (EDOT), ethanol pyridine, glycerol, dimethyl sulfoxide (DMSO) and (3-glycidyloxypropyl) trimethoxysilane (GOPS) were purchased from Sigma (Sweden) and used as received. PEDOT:PSS (Clevios, PH1000) and iron(III) tosylate (54 wt% in butanol, Clevios CB-54) were purchased from Heraeus Holding GmbH. Experiments were carried out with deionized water.

6.2 Procedures

A GC (disk, diam. 5 mm) was used as the substrate for film loadings. The GC was polished using 0.3 μm and 0.05 μm alumina powder (CH Instruments, Inc.) and rinsed with DI water.

PEDOT:PSS films on the GC were prepared by drop-casting of 5 μL of the polymer blend (PEDOT:PSS, DMSO, 10 mM glycerol, GOPS (94 wt%, 4 wt%, 1.5 wt% and 0.5 wt%, respectively)), followed by drying in an oven (75 °C) for 30 minutes.

PEDOT:Tos films were first prefabricated by vapour phase polymerisation. First, 5 mL of iron(III) *p*-toluenesulfonate (40% solution in *n*-butanol) and 0.2 mL of pyridine were mixed and stirred for 1 hour. Next, the oxidant solution was spin-coated onto the metal-modified glass described above and then heated up for 30 seconds at 60 °C before putting in a vacuum chamber, and three drops of the EDOT monomer were added onto two glass slides and placed in a hotplate by the side of the sample. The polymerization was completed under a vacuum condition of 60 mm Hg, after 1 hour followed by heating for 2 minutes at 60 °C. The samples were gently rinsed in ethanol and dried under nitrogen flow before use. Then, the PEDOT:Tos films were gently lifted up in water and attached to the GC followed by drying under nitrogen flow and heating (60 °C for 30 min).

Britton–Robinson buffers (Table 1) were used as the universal buffer systems in all experiments with buffered

 This journal is © The Royal Society of Chemistry and the Centre National de la Recherche Scientifique 2025

Open Access Article. Published on 06 February 2025. Downloaded on 4/1/2026 5:58:52 PM.
This article is licensed under a Creative Commons Attribution 3.0 Unported Licence.

Table 1 The compositions of the Britton–Robinson buffers

pH	Concentration, g L^{-1}					Molar concentration, M					Total concentration, M
	NaOH	CH_3COOH	H_3PO_4	H_3BO_3	KCl	NaOH	CH_3COOH	H_3PO_4	H_3BO_3	KCl	
2.09	0.558	2.234	3.647	2.301	5.964	0.014	0.037	0.037	0.038	0.08	0.206
2.87	1.191	2.044	3.336	2.105	5.203	0.03	0.034	0.034	0.035	0.07	0.203
4.1	1.6	1.922	3.136	1.979	4.562	0.04	0.032	0.032	0.032	0.06	0.196
5.02	2.074	1.779	2.904	1.832	3.683	0.052	0.03	0.03	0.03	0.05	0.192
6.09	2.386	1.686	2.751	1.736	2.959	0.06	0.03	0.028	0.029	0.04	0.187
7	2.754	1.575	2.57	1.622	1.804	0.07	0.026	0.026	0.027	0.024	0.173
7.96	3	1.501	2.45	1.546	0.357	0.075	0.025	0.025	0.025	0.005	0.155
8.95	3.224	1.434	2.34	1.477	0	0.081	0.024	0.024	0.024	0	0.153
9.91	3.493	1.353	2.208	1.393	0	0.087	0.023	0.023	0.023	0	0.156
10.88	3.616	1.316	2.148	1.355	0	0.09	0.022	0.022	0.022	0	0.156
11.98	4	1.201	1.96	1.237	0	0.1	0.02	0.02	0.02	0	0.16

media.[68,69] The actual pH values of the solutions were confirmed by pH measurements.

6.3 Methods

A BioLogic SP200 potentiostat was used for all the electrochemical measurements. An Ag/AgCl electrode in 3 M KCl and a Pt mesh were used as the reference electrode and counter electrode, respectively. 85% of ohmic drop correction (determined by a high-frequency impedance (50 kHz and 20 mV amplitude)) was performed prior to each voltammetry measurement on film working electrodes. A RDE (GC disk 5 mm diam., Pine Research Instrumentation Inc., USA) was used. The RDE was modified with PEDOT:PSS films *via* blend drop-casting followed by heating (60 °C for 30 minutes). PEDOT:Tos films were prepared first as described above followed by gentle transfer onto the RDE in water. Then, the RDE was dried under nitrogen flow followed by heating (60 °C for 30 minutes).

Author contributions

Canyan Che contributed to experimental analysis, data curation, formal analysis, original draft and review & editing; Viktor Gueskine & Martin Sjödin supported in conceptualization and methodology validation; Alexander Pozhitkov supported in data curation; Magnus Berggren, Yuguang Ma, and Reverant Crispin contributed to funding acquisition and supervision; Mikhail Vagin contributed to conceptualization, data curation, formal analysis, methodology, original draft and review & editing.

Data availability

Data are available on request from the corresponding author and first author.

Conflicts of interest

There are no conflicts to declare.

Acknowledgements

The authors thank VINNOVA (Digital Cellulose Center, 308634, 308635), the Knut and Alice Wallenberg Foundation (KAW 2019.0604, KAW 2021.0195), Wallenberg Wood Science Center (WWSC), Wallenberg Initiative Materials Science for Sustainability (WISE), Wallenberg Launchpad (WALP), the Swedish Energy Agency (52023-1), Vetenskaprådet (2016-05990), and The Foreign Experts Program of the Ministry of Science and Technology of China (G2022163014L) for financial funding.

References

1 M. Berggren, E. D. Głowacki, D. T. Simon, E. Stavrinidou and K. Tybrandt, In Vivo Organic Bioelectronics for Neuromodulation, *Chem. Rev.*, 2022, **122**(4), 4826–4846.
2 G. J. P. Allen, R. P. Henry and D. Weihrauch, Chapter 3 - Acid-base regulation. *In Ecophysiology of the European Green Crab (Carcinus Maenas) and Related Species*, ed. D. Weihrauch and I. J. McGaw, Academic Press, 2024, pp. 47–80.
3 S. Magder, A. Magder and G. Samoukovic, Intracellular pH regulation and the acid delusion, *Can. J. Physiol. Pharmacol.*, 2020, **99**(6), 561–576.
4 W. Aoi, X. Zou, J. B. Xiao and Y. Marunaka, Body Fluid pH Balance in Metabolic Health and Possible Benefits of Dietary Alkaline Foods, *eFood*, 2020, **1**(1), 12–23.
5 J. L. Seifter and H. Y. Chang, Extracellular Acid-Base Balance and Ion Transport Between Body Fluid Compartments, *Physiology*, 2017, **32**(5), 367–379.
6 L. Q. Chen, C. M. Howison, J. J. Jeffery, I. F. Robey, P. H. Kuo and M. D. Pagel, Evaluations of Extracellular pH within In Vivo Tumors Using acidoCEST MRI, *Magn. Reson. Med.*, 2014, **72**(5), 1408–1417.
7 M. M. Chen, C. Y. Chen, Z. W. Shen, X. L. Zhang, Y. Z. Chen, F. F. Lin, X. L. Ma, C. Y. Zhuang, Y. F. Mao, H. C. Gan, P. D. Chen, X. D. Zong and R. H. Wu, Extracellular pH is a biomarker enabling detection of breast cancer and liver cancer using CEST MRI, *Oncotarget*, 2017, **8**(28), 45759–45767.
8 S. Magder, A. Magder and G. Samoukovic, Intracellular pH regulation and the acid delusion, *Can. J. Physiol. Pharmacol.*, 2021, **99**(6), 561–576.

Open Access Article. Published on 06 February 2025. Downloaded on 4/1/2026 5:58:52 PM.
This article is licensed under a Creative Commons Attribution 3.0 Unported Licence.

9 Y. Liu, K. A. White and D. L. Barber, Intracellular pH Regulates Cancer and Stem Cell Behaviors: A Protein Dynamics Perspective, *Front. Oncol.*, 2020, **10**, 1401.
10 B. E. Conway, *Electrochemical Supercapacitors*, Springer, US, 1999.
11 W. Aoi and Y. Marunaka, Importance of pH Homeostasis in Metabolic Health and Diseases: Crucial Role of Membrane Proton Transport, *BioMed Res. Int.*, 2014, 98986.
12 G. Ellison, J. V. Straumfjord and J. P. Hummel, Buffer Capacities of the Human Blood and Plasma, *Clin. Chem.*, 1958, **4**(6), 452–461.
13 B. K. Siesjo and U. Ponten, The Buffer Capacity of Brain Tissue and of Equivalent Systems, *Ann. N. Y. Acad. Sci.*, 1966, **133**(1), 180–189.
14 Y. Li, S. Park, K. Sarang, H. Mei, C.-P. Tseng, Z. Hu, D. Zhu, X. Li, J. Lutkenhaus and R. Verduzco, Mixed Ionic–Electronic Conduction Increases the Rate Capability of Polynaphthalenediimide for Energy Storage, *ACS Polym. Au*, 2023, **3**(3), 267–275.
15 E. S. Muckley, C. B. Jacobs, K. Vidal, J. P. Mahalik, R. Kumar, B. G. Sumpter and I. N. Ivanov, New Insights on Electro-Optical Response of Poly(3,4-ethylenedioxythiophene):Poly(styrenesulfonate) Film to Humidity, *ACS Appl. Mater. Interfaces*, 2017, **9**(18), 15880–15886.
16 D. Vonlanthen, P. Lazarev, K. A. See, F. Wudl, A. J. Heeger and A. Stable Polyaniline-Benzoquinone-Hydroquinone Supercapacitor, *Adv. Mater.*, 2014, **26**(30), 5095–5100.
17 B. D. Paulsen, K. Tybrandt, E. Stavrinidou and J. Rivnay, Organic mixed ionic–electronic conductors, *Nat. Mater.*, 2019, 13–26.
18 J. Rivnay, S. Inal, B. A. Collins, M. Sessolo, E. Stavrinidou, X. Strakosas, C. Tassone, D. M. Delongchamp and G. G. Malliaras, Structural control of mixed ionic and electronic transport in conducting polymers, *Nat. Commun.*, 2016, **7**, 11287.
19 J. B. Hu, A. Stein and P. Buhlmann, Rational design of all-solid-state ion-selective electrodes and reference electrodes, *TrAC, Trends Anal. Chem.*, 2016, **76**, 102–114.
20 M. Vagin, C. Che, V. Gueskine, M. Berggren and X. Crispin, Ion-Selective Electrocatalysis on Conducting Polymer Electrodes: Improving the Performance of Redox Flow Batteries, *Adv. Funct. Mater.*, 2020, **30**(52), 2007009.
21 G. Schiavone, X. Kang, F. Fallegger, J. Gandar, G. Courtine and S. P. Lacour, Guidelines to Study and Develop Soft Electrode Systems for Neural Stimulation, *Neuron*, 2020, **108**(2), 238–258.
22 A. R. Harris and G. G. Wallace, Organic Electrodes and Communications with Excitable Cells, *Adv. Funct. Mater.*, 2018, **28**(12), 1700587.
23 J. Isaksson, P. Kjäll, D. Nilsson, N. Robinson, M. Berggren and A. Richter-Dahlfors, Electronic control of Ca^{2+} signalling in neuronal cells using an organic electronic ion pump, *Nat. Mater.*, 2007, **6**(9), 673–679.
24 D. Khodagholy, T. Doublet, P. Quilichini, M. Gurfinkel, P. Leleux, A. Ghestem, E. Ismailova, T. Hervé, S. Sanaur, C. Bernard and G. G. Malliaras, In vivo recordings of brain activity using organic transistors, *Nat. Commun.*, 2013, **4**(1), 1575.
25 S. p P. Lacour, G. Courtine and J. Guck, Materials and technologies for soft implantable neuroprostheses, *Nat. Rev. Mater.*, 2016, **1**, 16063.
26 Y. Liu, J. Liu, S. Chen, T. Lei, Y. Kim, S. Niu, H. Wang, X. Wang, A. M. Foudeh, J. B. H. Tok and Z. Bao, Soft and elastic hydrogel-based microelectronics for localized low-voltage neuromodulation, *Nat. Biomed. Eng.*, 2019, **3**(1), 58–68.
27 Q. Gao, F. Sun, Y. Li, L. Li, M. Liu, S. Wang, Y. Wang, T. Li, L. Liu, S. Feng, X. Wang, S. Agarwal and T. Zhang, Biological Tissue-Inspired Ultrasoft, Ultrathin, and Mechanically Enhanced Microfiber Composite Hydrogel for Flexible Bioelectronics, *Nano-Micro Lett.*, 2023, **15**(1), 139.
28 S. M. Richardson-Burns, J. L. Hendricks, B. Foster, L. K. Povlich, D. H. Kim and D. C. Martin, Polymerization of the conducting polymer poly(3,4-ethylenedioxythiophene) (PEDOT) around living neural cells, *Biomaterials*, 2007, **28**(8), 1539–1552.
29 Y. Xiang, Y. Zhao, T. Cheng, S. Sun, J. Wang and R. Pei, Implantable Neural Microelectrodes: How to Reduce Immune Response, *ACS Biomater. Sci. Eng.*, 2024, **10**(5), 2762–2783.
30 K. Wijeratne, U. Ail, R. Brooke, M. Vagin, X. Liu, M. Fahlman and X. Crispin, Bulk electronic transport impacts on electron transfer at conducting polymer electrode–electrolyte interfaces, *Proc. Natl. Acad. Sci. U. S. A.*, 2018, **115**(47), 11899–11904.
31 K. Xu, H. Sun, T. P. Ruoko, G. Wang, R. Kroon, N. B. Kolhe, Y. Puttisong, X. Liu, D. Fazzi, K. Shibata, C. Y. Yang, N. Sun, G. Persson, A. B. Yankovich, E. Olsson, H. Yoshida, W. M. Chen, M. Fahlman, M. Kemerink, S. A. Jenekhe, C. Müller, M. Berggren and S. Fabiano, Ground-state electron transfer in all-polymer donor-acceptor heterojunctions, *Nat. Mater.*, 2020, **19**(7), 738–744.
32 N. Sepat, M. Vagin, S. Carli, E. Marchini, S. Caramori, Q. Zhang, S. Braun, Z. Wu, P. Ding, K. Wijeratne, I. Petsagkourakis, U. Ail, E. Pavlopoulou, T.-P. Ruoko, S. Fabiano, K. Tybrandt, M. Fahlman, R. Crispin, M. Berggren, V. Gueskine and I. Engquist, Decoupling Conductivity, Heterogeneous Electron Transfer Rate, and Diffusion in Organic Molecular Electrocatalysis: Oxygen Reduction Reaction on Poly(3,4-ethylenedioxythiophene), *Small*, 2024, 2409471n/a (n/a).
33 S. De Causmaecker, J. S. Douglass, A. Fantuzzi, W. Nitschke and A. W. Rutherford, Energetics of the exchangeable quinone, QB, in Photosystem II, *Proc. Natl. Acad. Sci. U. S. A.*, 2019, **116**(39), 19458–19463.
34 Y. Sugo, H. Tamura and H. Ishikita, Electron Transfer Route between Quinones in Type-II Reaction Centers. The, *J. Phys. Chem. B*, 2022, **126**(46), 9549–9558.
35 M. Sarewicz and A. Osyczka, Electronic connection between the quinone and cytochrome *C* redox pools and its role in regulation of mitochondrial electron transport and redox signaling, *Physiol. Rev.*, 2015, **95**(1), 219–243.

 This journal is © The Royal Society of Chemistry and the Centre National de la Recherche Scientifique 2025

Open Access Article. Published on 06 February 2025. Downloaded on 4/1/2026 5:58:52 PM.
This article is licensed under a Creative Commons Attribution 3.0 Unported Licence.

36 K. T. Ngo, E. L. Varner, A. C. Michael and S. G. Weber, Monitoring Dopamine Responses to Potassium Ion and Nomifensine by in Vivo Microdialysis with Online Liquid Chromatography at One-Minute Resolution, *ACS Chem. Neurosci.*, 2017, **8**(2), 329–338.

37 M. Luo, X. G. Chenran Zhang, Y. Yang, W. Yue, I. Zhitomirsky and K. Shi, Overcoming Obstacles in Zn-Ion Batteries Development: Application of Conductive Redox-Active Polypyrrole/Tiron Anolyte Interphase, *Adv. Funct. Mater.*, 2023, **33**(47), 2305041.

38 F. Hasan, V. Mahanta and A. A. A. Abdelazeez, Quinones for Aqueous Organic Redox Flow Battery: A Prospective on Redox Potential, Solubility, and Stability, *Adv. Mater. Interfaces*, 2023, **10**(24), 2300268.

39 Y. Zhou, Q. Wei, L. Xiao, C. Meng, Q. Yin, S. Song, Y. He, R. Qiang, Y. Yang, Z. Li and Z. Hu, Quinone-Enriched Polymer with a Large π-Conjugated Structure for High-Energy Supercapacitors: Synthesis and Electrochemical Assessment, *Energy Fuels*, 2024, **38**(8), 7399–7411.

40 J. Edberg, O. Inganäs, I. Engquist and M. Berggren, Boosting the capacity of all-organic paper supercapacitors using wood derivatives, *J. Mater. Chem. A*, 2018, **6**(1), 145–152.

41 C. Che, M. Vagin, U. Ail, V. Gueskine, J. Phopase, R. Brooke, R. Gabrielsson, M. P. Jonsson, W. C. Mak, M. Berggren and X. Crispin, Twinning Lignosulfonate with a Conducting Polymer via Counter-Ion Exchange for Large-Scale Electrical Storage, *Adv. Sustainable Syst.*, 2019, **3**(9), 1900039.

42 C. Han, H. Li, R. Shi, T. Zhang, J. Tong, J. Li and B. Li, Organic quinones towards advanced electrochemical energy storage: recent advances and challenges, *J. Mater. Chem. A*, 2019, **7**(41), 23378–23415.

43 S. X. Wang and J. H. Waite, Catechol redox maintenance in mussel adhesion, *Nat. Rev. Chem.*, 2025, DOI: **10.1038/s41570-024-00673-4**.

44 Z. M. Robole, K. L. Rahn, B. J. Lampkin, R. K. Anand and B. VanVeller, Tuning the Electrochemical Redox Potentials of Catechol with Boronic Acid Derivatives. The, *J. Org. Chem.*, 2019, **84**(4), 2346–2350.

45 Y. Xu, Y.-H. Wen, J. Cheng, G.-P. Cao and Y.-S. Yang, A study of tiron in aqueous solutions for redox flow battery application, *Electrochim. Acta*, 2010, **55**(3), 715–720.

46 S. Goia, G. W. Richings, M. A. P. Turner, J. M. Woolley, J. J. Tully, S. J. Cobb, A. Burriss, B. R. Robinson, J. V. Macpherson and V. G. Stavros, Ultrafast Spectroelectrochemistry of the Catechol/o-Quinone Redox Couple in Aqueous Buffer Solution, *ChemPhotoChem*, 2024, **8**(9), e202300325.

47 W. Lee, G. Park and Y. Kwon, High power density near-neutral pH aqueous redox flow batteries using zinc chloride and 4,5-dihydroxy-1,3-benzenedisulfonate as redox couple with polyethylene glycol additive, *Int. J. Energy Res.*, 2021, **45**(7), 10024–10042.

48 B. L. Groenendaal, F. Jonas, D. Freitag, H. Pielartzik and J. R. Reynolds, Poly(3,4-ethylenedioxythiophene) and its derivatives: Past, present, and future, *Adv. Mater.*, 2000, **12**(7), 481–494.

49 M. T. Huynh, C. W. Anson, A. C. Cavell, S. S. Stahl and S. Hammes-Schiffer, Quinone 1 e– and 2 e–/2 H+ Reduction Potentials: Identification and Analysis of Deviations from Systematic Scaling Relationships, *J. Am. Chem. Soc.*, 2016, **138**(49), 15903–15910.

50 E. Laviron, Electrochemical reactions with protonations at equilibrium: Part VIII. The 2 e, 2H+ reaction (nine-member square scheme) for a surface or for a heterogeneous reaction in the absence of disproportionation and dimerization reactions, *J. Electroanal. Chem. Interfacial Electrochem.*, 1983, **146**(1), 15–36.

51 S. Steenken and P. Neta, Electron-transfer rates and equilibria betweeen substituted phenoxide ions and phenoxyl radicals, *J. Phys. Chem.*, 1979, **83**(9), 1134–1137.

52 Q. Q. Lin, Q. Li, C. Batchelor-McAuley and R. G. Compton, Two-Electron, Two-Proton Oxidation of Catechol: Kinetics and Apparent Catalysis, *J. Phys. Chem. C*, 2015, **119**(3), 1489–1495.

53 M. R. Deakin, P. M. Kovach, K. J. Stutts and R. M. Wightman, Heterogeneous mechanisms of the oxidation of catechols and ascorbic acid at carbon electrodes, *Anal. Chem.*, 1986, **58**(7), 1474–1480.

54 M. R. Deakin and R. M. Wightman, The kinetics of some substatuted catechol/ortho-quinone couples at a carbon paste electrode, *J. Electroanal. Chem.*, 1986, **206**(1–2), 167–177.

55 E. Laviron, Electrochemical reactions with protonations at equilibrium. 10. The kinetics of para-benzoquinone hydroquinone couple on a platinum electrode, *J. Electroanal. Chem.*, 1984, **164**(2), 213–227.

56 S. Steenken and P. Oneill, Oxidative demethoxylation of methoxylated phenols and hydroxybenzoic acids by OH radical - in-situ electron spin resonance cunductometric pulse radiolysis and product andlysis study, *J. Phys. Chem.*, 1977, **81**(6), 505–508.

57 G. Schwarzenbach and A. Willi, Metallindikatoren III. Die Komplexbildung der Brenzcatechin-3,5-disulfosäure (= Tiron) mit dem Eisen(III)-ion, *Helv. Chim. Acta*, 1951, **34**(2), 528.

58 L. Hoober-Burkhardt, S. Krishnamoorthy, B. Yang, A. Murali, A. Nirmalchandar, G. K. S. Prakash and S. R. Narayanan, A New Michael-Reaction-Resistant Benzoquinone for Aqueous Organic Redox Flow Batteries, *J. Electrochem. Soc.*, 2017, **164**(4), A600.

59 A. Kiani, J.-B. Raoof, D. Nematollahi and R. J. E. Ojani, Electrochemical Study of Catechol in the Presence of Dibuthylamine and Diethylamine in Aqueous Media: Part 1. Electrochemical Investigation, *Electroanalysis*, 2005, **17**, 1755–1760.

60 B. Yang, L. Hoober-Burkhardt, S. Krishnamoorthy, A. Murali, G. K. S. Prakash and S. R. Narayanan, High-Performance Aqueous Organic Flow Battery with Quinone-Based Redox Couples at Both Electrodes, *J. Electrochem. Soc.*, 2016, **163**(7), A1442.

61 M. E. Joy, A. K. Tripathi, R. Das, R. Maurya and M. Neergat, Electrochemical Impedance Spectroscopy Investigation of

Open Access Article. Published on 06 February 2025. Downloaded on 4/1/2026 5:58:52 PM.
This article is licensed under a Creative Commons Attribution 3.0 Unported Licence.

Organic Redox Reactions (*p*-Benzoquinone/Hydroquinone Couple)-Implications to Organic Redox Flow Batteries, *J. Phys. Chem. C*, 2021, **125**(50), 27556–27565.

62 X. Crispin, F. L. E. Jakobsson, A. Crispin, P. C. M. Grim, P. Andersson, A. Volodin, C. van Haesendonck, M. Van der Auweraer, W. R. Salaneck and M. Berggren, The origin of the high conductivity of poly(3,4-ethylenedioxythiophene)-poly(styrenesulfonate) (PEDOT-PSS) plastic electrodes, *Chem. Mater.*, 2006, **18**(18), 4354–4360.

63 G. Ma, N. Jiang, Y. Zhang, D. Song, B. Qiao, Z. Xu, S. Zhao and Z. Liang, Buffering Donor Shuttles in Proton-Coupled Electron Transfer Kinetics for Electrochemical Hydrogenation of Hydroxyacetone to Propylene Glycol, *J. Am. Chem. Soc.*, 2024, **146**(33), 23194–23204.

64 J. Wang, L. Wang, Y. Wang, W. Yang, L. Jiang and E. Wang, Effect of buffer capacity on electrochemical behavior of dopamine and ascorbic acid, *J. Electroanal. Chem.*, 2007, **601**(1–2), 107–111.

65 M. Vagin, C. Y. Che, V. Gueskine, M. Berggren and X. Crispin, Ion-Selective Electrocatalysis on Conducting Polymer Electrodes - Improving the Performance of Redox Flow Batteries, *Adv. Funct. Mater.*, 2020, **30**, 52.

66 S. Fletcher, Tafel slopes from first principles, *J. Solid State Electrochem.*, 2009, **13**(4), 537–549.

67 D. Voiry, M. Chhowalla, Y. Gogotsi, N. A. Kotov, Y. Li, R. M. Penner, R. E. Schaak and P. S. Weiss, Best Practices for Reporting Electrocatalytic Performance of Nanomaterials, *ACS Nano*, 2018, **12**(10), 9635–9638.

68 H. T. S. Britton and R. A. Robinson, CXCVIII.—Universal buffer solutions and the dissociation constant of veronal, *J. Chem. Soc.*, 1931, 1456–1462.

69 C. Mongay and V. Cerda, Britton-Robinson Buffer of known Ionic Strength, *Ann. Chim.*, 1974, **64**, 409–412.

 This journal is © The Royal Society of Chemistry and the Centre National de la Recherche Scientifique 2025